Semiannual Technical Summary

Solid Electrolytes and Photoelectrolysis

31 December 1974

Lincoln Laboratory

MASSACHUSETTS INSTITUTE OF TECHNOLOGY
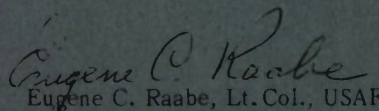
LEXINGTON, MASSACHUSETTS

The work reported in this document was performed at Lincoln Laboratory, a center for research operated by Massachusetts Institute of Technology. This work was sponsored by the Advanced Research Projects Agency of the Department of Defense under Air Force Contract F19628-73-C-0002 (ARPA Order 2696).

This report may be reproduced to satisfy needs of U.S. Government agencies.

The views and conclusions contained in this document are those of the contractor and should not be interpreted as necessarily representing the official policies, either expressed or implied, of the Defense Advanced Research Projects Agency of the United States Government.

This technical report has been reviewed and is approved for publication.

FOR THE COMMANDER

Eugene C. Raabe, Lt. Col., USAF
Chief, ESD Lincoln Laboratory Project Office

MASSACHUSETTS INSTITUTE OF TECHNOLOGY

LINCOLN LABORATORY

SOLID ELECTROLYTES AND PHOTOELECTROLYSIS

SEMIANNUAL TECHNICAL SUMMARY REPORT
TO THE
ADVANCED RESEARCH PROJECTS AGENCY

1 MARCH — 31 DECEMBER 1974

ISSUED 10 APRIL 1975

LEXINGTON   MASSACHUSETTS

ABSTRACT

Three classes of cubic skeleton structures are explored for fast Na^+-ion transport for use as solid electrolytes in Na-S batteries. The cubic $KSbO_3$ structure consists of an $(SbO_3)^-$ skeleton having $\langle 111 \rangle$ tunnels intersecting at origin and body-center positions. $NaSbO_3$ and $NaSbO_3 \cdot (1/6)$ NaF disks of ca. 95 percent theoretical density give a Na^+-ion resistivity at 300°C of $\rho_{300} \simeq 13$ Ω-cm and an activation energy $\mathcal{E}_a \simeq 0.35$ eV. The defect-pyrochlore structures have a B_2X_6 skeleton of corner-shared octahedra with alkali ions in 8b positions. At a critical lattice parameter, K^+ ions have an equal site preference for 8b and 16d positions, but determination of the critical parameter and exploitation of it are hampered by a critical parameter for hydration to occur. Preliminary investigations of aluminosilicates having the carnegieite structure show promise, but a $\rho_{300} \simeq 610$ Ω-cm is the best that has been achieved to date.

We have investigated the use of inexpensive, n-type hot-pressed TiO_2 powders as the working photocatalytic electrode for achieving photoelectrolysis of water. TiO_2 was selected because it is the lowest gap n-type semiconductor that, under illumination at an interface with water, evolves O_2 and does not decompose. A study of the physics and electrochemistry of a photoelectrolysis cell consisting of TiO_2 as the anode and platinized-platinum as the cathode led to an optimization of the parameters of the system by appropriately bending the bands in TiO_2 and shifting the Fermi level of the ions in the solution. Under these conditions an external quantum efficiency of 60 percent was measured and, from this, an internal quantum efficiency close to 100 percent was estimated.

CONTENTS

I. SOLID ELECTROLYTES: ALKALI-ION TRANSPORT IN SKELETON STRUCTURES

A. TECHNICAL PROBLEM

A practical Na-S battery would have many significant applications. A key component is a durable solid-electrolyte membrane that passes Na$^+$ ions at practical temperatures. A number of efforts are aimed at improving ceramic membranes of the layer compounds β- and β''-alumina. This study would identify substitute solid-electrolyte materials by exploring cubic "skeleton" structures for fast alkali-ion transport.

B. GENERAL METHODOLOGY

Task 1 is to select candidate crystallographic structures. We have chosen cubic "skeleton" structures so as to avoid the disadvantages of layer structures. These structures have a rigid skeleton (subarray) penetrated by intersecting tunnels in which alkali ions can move.

Task 2 is to prepare the candidate materials and to characterize them both chemically and structurally.

Task 3 is to prepare dense ceramic disks for transport measurements. This task is not trivial if the desired phases are metastable.

Task 4 is to measure the transport properties.

Task 5 is to measure performance life under operational conditions.

C. TECHNICAL RESULTS

Three structural classes have been investigated: the Im3 phase of high-pressure $K^+(SbO_3)^-$, the defect pyrochlores represented by $Rb^+(MgAlF_6)^-$, and aluminosilicates with the skeleton of carnegieite: $Na^+(AlSiO_4)^-$. Hot-pressing stages have been set up for the preparation of dense ceramic disks, and a pulse-measurement apparatus has been built to supplement the conventional bridge methods used to measure the transport properties.

1. Im3 phase. A metastable cubic phase of $NaSbO_3$ was obtained from high-pressure $KSbO_3$ by ion exchange in molten $NaNO_3$. Ceramic disks over 95 percent dense were obtained with the aid of 2w/o $NaNH_2$ as a flux in the hot-pressing step. Transport measurements showed negligible electronic conductivity and a resistivity for Na$^+$-ion transport at 300 °C of $\rho_{300} \approx 18$ Ω-cm, about a factor of three larger than β-alumina. The temperature dependence of the resistivity had an activation energy $\mathcal{E}_a \simeq 0.35$ eV, about a factor of two larger than β-alumina. Since x-ray measurements showed no charge density at the tunnel intersections, we prepared $NaSbO_3 \cdot (1/6)$ NaF, which had F-ions at these sites. The Na$^+$-ion transport was slightly improved.

These measurements demonstrate that fast alkali-ion transport can be obtained in cubic structures and that use of the entire crystal for transport improves the preexponential factor in the resistivity. Lowering of $\mathcal{E}_a$ by a factor of two would give transport properties superior to those of β-alumina.

2. <u>Pyrochlores.</u> The pyrochlore structure, corresponding to generalized chemical formula $A_2B_2X_6X'$, has a B_2X_6 skeleton. The interpenetrating A_2X' subarray has A cations in 16d and X' anions in 8b positions of the Fd3m cell if the origin is taken at a B cation. Defect pyrochlores $A^+(B_2X_6)^-$ can be prepared directly if the A^+ ion is large enough to occupy the 8b positions, i.e., A = Cs, Rb, and sometimes K. The K and Na analogues can be prepared by ion exchange of the Rb compounds. We have initiated experiments on three series: $A^+(TaWO_6)^-$, $A^+(Ta_2O_5F)^-$, and $A^+(MgAlF_6)^-$. Work to date indicates that there is a critical cell size at which K^+ ions have an equal stability in either 16d or 8b sites, the ideal condition of fast ion transport. Unfortunately, water also enters the structure under these conditions. Although the transport properties of the Na analogue "$NaTa_2O_5F$" appear promising, we have not yet been able to determine the charge-compensation mechanism responsible for an apparent Na^+-ion excess.

3. <u>Aluminosilicates.</u> Experiments on $Na_4Al_2Si_2O_9$ and $Na_3Al_2Si_2O_{8.5}$, each with the carnegieite skeleton, are promising, but as yet very preliminary.

D. IMPLICATIONS FOR FURTHER RESEARCH

Our results demonstrate that cubic "skeleton" structures can provide alkali-ion transport comparable to that of β-alumina and that superior transport properties may be achievable. However, the number of candidate structures is limited, and it appears that fast ion transport could be limited to metastable phases, thus complicating the fabrication of dense ceramic membranes. Optimization of the cell size of $NaSbO_3 \cdot (1/6) NaF$ should be attempted before life tests are initiated. Considerably more work on the pyrochlores and aluminosilicates is needed.

II. PHOTOELECTROLYSIS

A. TECHNICAL PROBLEM

To use solar energy to photoelectrolyze water into H_2 and O_2, i.e., into fuel.

B. GENERAL METHODOLOGY

Our approach has been primarily experimental, with enough theoretical work to aid in the interpretation of our experimental results and to suggest new experiments and courses of action.

Our first objective was to study n-type hot-pressed TiO_2 powders, which are less expensive and easier to fabricate than single crystals, in order to compare the performance of the powders to that of the single crystals. To accomplish this required: (1) adjustment of the parameters of the photoelectrolysis cell so as to make the reaction at the TiO_2 electrode the rate-limiting step, and (2) further optimization of the variables to obtain the highest efficiency. These tasks involved measurements of:

    (1) Flat-band potential as a function of pH in order to determine the band bending,

    (2) Current-voltage characteristics as a function of photon energy of light and electrolyte pH,

    (3) Capacitance-voltage characteristics as a function of electrolyte pH,

(4) Photoelectrolysis current as a function of platinized-platinum area and also intensity of light, and

(5) Effect of stirring to replenish the depleted ions near the electrodes during high-current discharge.

Since the energy gap of TiO_2 is 3eV, which is higher than the peak of the sun's radiation (~2.5eV), this material is not optimum for solar photoelectrolysis. Therefore, there is need to find materials that have a smaller energy gap and yet still are chemically stable under anodic polarization. This is being attacked with three approaches, namely,

(1) Search for new n-type semiconductors with a smaller energy gap,

(2) Doping TiO_2 appropriately to decrease the effective gap, and

(3) Alloying TiO_2 with a metallurgically and chemically compatible solid of a smaller energy gap.

C. TECHNICAL RESULTS

As a result of the information obtained from the basic measurements outlined in B, we have been able to optimize the variables of the system and demonstrate that the external quantum efficiency, i.e., the ratio of the number of electrons flowing in the external circuit to the number of photons impinging on the cell, is ~60 percent for photon energies $h\nu \sim 4eV$ and $pH \geqslant 4.7$. By taking into account the reflections at the various interfaces of the cell, as well as absorption of light by the electrolyte, we obtain an internal quantum efficiency of close to 100 percent. Even though the maximum quantum efficiency occurs at such a high energy in TiO_2, the measured efficiency, with this single electrode, for converting solar energy into fuel (H_2) energy is ~1 percent. This is to be compared with the best of the single-crystal solar cells, which convert solar energy to electrical energy with an efficiency of ~15 percent. (Polycrystalline solar cells have efficiencies ~5 percent.) By finding a material with a lower gap, we should be easily competitive with solar cells. Furthermore, photoelectrolysis offers the advantage of mobile storage of the fuel to be used later either for heat, propulsion, or generation of electricity (by means of a fuel cell).

D. IMPLICATIONS FOR FURTHER RESEARCH

Our results demonstrate that photoelectrolysis is a very promising method for collecting solar energy. Films of polycrystalline TiO_2 would be cheap and the generation of a fuel, hydrogen, greatly simplifies the storage problem. Moreover, hydrogen is, in itself, an extremely valuable commodity. Research in this area should therefore be pursued further.

Aside from finding a lower energy gap material for the anode, the platinum cathode needs to be replaced with a p-type semiconductor that is chemically stable and has a still smaller energy gap. Going to a semiconductor cathode will offer two advantages: (1) lower cost, and (2) higher efficiency, since with the use of semiconductor electrodes for both the anode and cathode, the energy gaps can be separately adjusted so as to use a larger part of the sun's spectrum.

I. SOLID ELECTROLYTES: ALKALI-ION TRANSPORT
IN SKELETON STRUCTURES

A. SKELETON STRUCTURES

1. Motivation

A practical Na-S cell would provide an energy density of ~100 Wh/lb. Mobile energy storage of this density would have a variety of important applications.

Two critical components of the Na-S cell are: (a) a suitable positive electrode (sodium polysulfide impregnated with carbon, $Na_xS:C$, is now used), and (b) a durable solid-electrolyte membrane that transports Na^+ ions with a low resistivity at a practical operating temperature. The study of alkali-ion transport in skeleton structures addresses itself to the solid electrolyte.

The discovery[1] that β-alumina, $(Na_2O)_{1+x}11Al_2O_3$, has a resistivity for Na^+-ion transport at 300°C of $\rho_{300} \simeq 5\Omega$-cm first alerted the technical community to the possibility of realizing a practical Na-S cell. Considerable effort has since been devoted to the fabrication of dense, durable ceramic membranes of this and closely related oxides. Nevertheless, repeated thermal cycling of these membranes causes cracking and the formation of leaks. Because β- and β''-alumina are layer compounds, they have a highly anisotropic thermal-expansion coefficient;[2] and thermal cycling of polycrystalline membranes introduces severe internal stresses. Moreover, confinement of the Na^+ ions to widely separated layers reduces sharply the fraction of the membrane volume that transports Na^+ ions. In order to avoid these two limitations of the β-alumina family, we decided to investigate alkali-ion transport in cubic structures. To obtain fast alkali-ion transport in a cubic structure, we decided to investigate cubic "skeleton" structures.

2. Examples of Skeleton Structures

A skeleton structure consists of a rigid subarray with intersecting channels, or tunnels, in which alkali ions can move in three dimensions. We are investigating three cubic skeleton structures: the Im3 phase of high-pressure $KSbO_3$, the defect-pyrochlore structure illustrated by $RbMgAlF_6$, and the carnegieite structure illustrated by high-temperature $NaAlSiO_4$.

a. <u>The Im3 phase</u>: A primitive-cubic Pn3 phase of $KSbO_3$ was first discovered by Spiegelberg.[3] The structure is composed of an $(SbO_3)^-$ subarray, the skeleton shown in Fig. I-1,
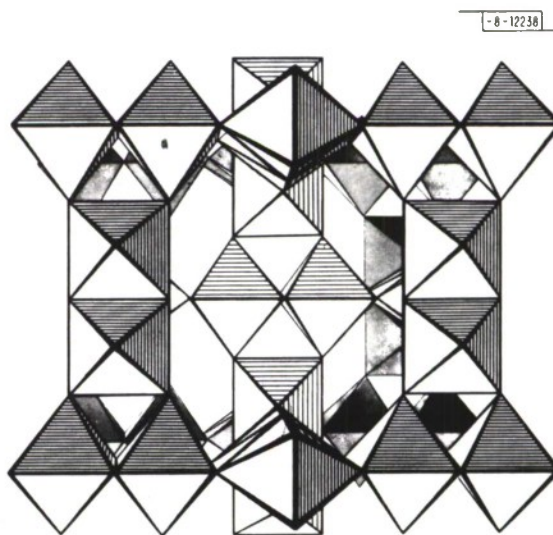

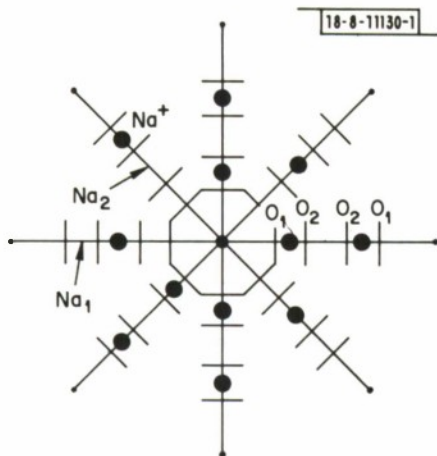Fig. I-1. The SbO_3 subarray of cubic $KSbO_3$.

Fig. I-2. Schematic representation of the eight $\langle 111 \rangle$ channels branching from the origin to the neighboring body-center positions in the disordered, cubic (Im3) phase of $KSbO_3$. In the ordered Pn3 structure, each singly occupied branch has an M_2 cation and the three nearest-neighbor branches are doubly occupied.
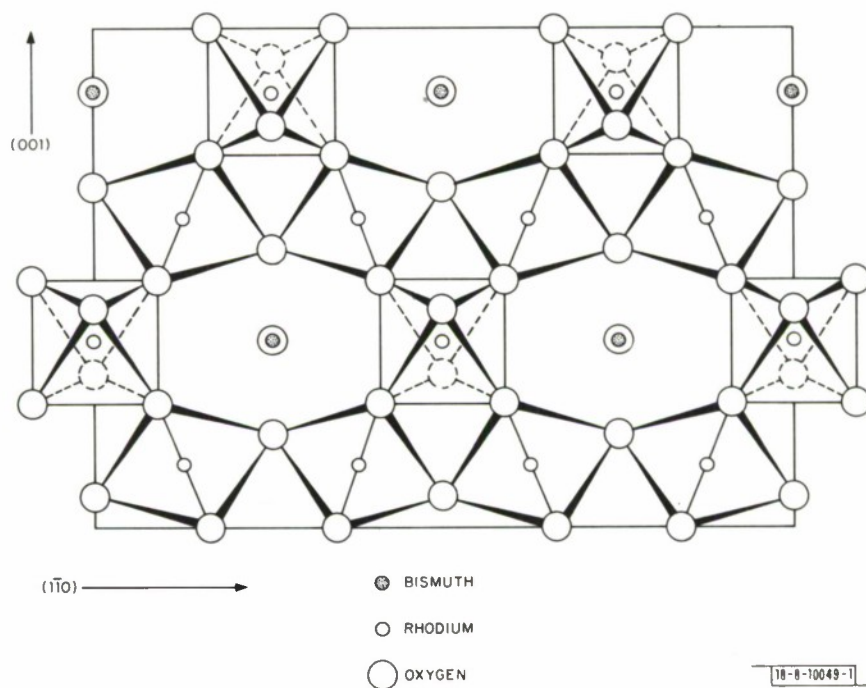

⊙ BISMUTH

○ RHODIUM

○ OXYGEN

Fig. I-3. The (110) projection of a cubic pyrochlore $Bi_2Rh_2O_7$, showing the B_2X_6 skeleton of corner-shared octahedra.

and an ordered arrangement of K^+ ions within $\langle 111 \rangle$ tunnels that traverse the skeleton, intersecting at the origin (center of front face in Fig. I-1) and body-center positions. The $(SbO_3)^-$ network is built up of pairs of edge-shared SbO_6 octahedra, forming Sb_2O_{10} clusters, that are connected by shared corners. The $\langle 111 \rangle$ tunnels are made up of face-shared octahedral sites that are compressed along the tunnel axis so as to provide a large spacing between the bridging oxygens within a shared face. The intersection sites at the origin and body-center positions are large octahedral interstices, and along any $\langle 111 \rangle$ axis three octahedral sites separate an origin and body-center position. Each of the shared faces along the tunnels consists of either O_1 or O_2 oxygen atoms. The order of the faces is O_1-O_2-O_2-O_1, see Fig. I-2, and the triangular area of an O_1 face is somewhat larger than that of an O_2 face. Octahedral sites having O_1 and O_2 faces are labeled M_1 sites, those with only O_2 faces are M_2 sites. The unit cell contains $K_{12}Sb_{12}O_{36}$, the K^+ ions occupying the M_1 and M_2 positions in an ordered manner so that each tunnel segment contains either two M_1 cations or one M_2 cation, and an M_2 cation has only M_1-cation nearest neighbors.

The stoichiometric, atmospheric-pressure phase of $KSbO_3$ has the rhombohedral ilmenite structure. During an investigation of the structural relationships among several $A^+B^{5+}O_3$ compounds, we[4] found a cubic high-pressure phase with space group Im3. This Im3 phase is similar to the primitive-cubic Pn3 phase discovered by Spiegelberg, but it contains K^+ ions randomly distributed among the M_1 and M_2 positions.

b. The defect-pyrochlore structure: The cubic pyrochlore structure corresponds to the chemical formula $A_2B_2X_6X'$, where A is a large cation and B is a smaller cation octahedrally coordinated by six X anions. The B_2X_6 subarray forms a skeleton of corner-shared octahedra, see Fig. I-3. Each X' anion is tetrahedrally coordinated by four A cations, and each A cation has two nearest neighbor X' ions on opposite sides and six X-ion neighbors forming a puckered ring perpendicular to the X'-A-X' axis. With space group Fd3m and the origin chosen at a B site, the A and X' positions are identified as 16d and 8b, the cubic unit cell containing $A_{16}B_{16}X_{48}X'_8$. (The B and X positions are the 16c and 48f positions of the space group.)

Babel et al.[5] prepared a number of fluorides $A^+B^{2+}B'^{3+}F_6$, where A = Cs, Rb, or K. These fluorides have a $B^{2+}B'^{3+}F_6$ skeleton identical to the B_2X_6 pyrochlore skeleton, the B and B' atoms being randomly distributed. In place of the A_2X' subarray of a pyrochlore, only the 8b positions are occupied by a large A^+ cation. Singer[6] suggested to us that these defect pyrochlores might represent cubic skeleton structures of the type we wished to investigate. We recognized that this suggestion would be valid provided vacancies could be established on the 8b sites either by stabilizing $A^+_{1-x}B^{2+}_{1-x}B'^{3+}_{1+x}F_6$ compounds with the same structure or by obtaining the phase with a lattice parameter conducive to random occupancy of 8b and 16d positions.

c. Carnegieites: The aluminosilicates are classic skeleton structures. The zeolites, for example, form molecular sieves. As these latter structures are stabilized by water, they are unsuitable for solid electrolytes that are to be in contact with molten alkali metal. Moreover, the openings are too large for optimal alkali-ion transport. The high-temperature form of $NaAlSiO_4$, carnegieite, is a more interesting possibility.

Carnegieite has a cubic $(AlSiO_4)^-$ skeleton having the structure of cubic SiO_2, see Fig. I-4. In the idealized structure, the Al and Si atoms form a cubic zincblende array with oxygen atoms on every Al-Si bond axis. This arrangement provides a network of corner-shared tetrahedra that, in the real carnegieite structure, becomes distorted to a primitive-cubic array by interaction with the Na^+ ions in the large voids about the body-center and edge-center positions.
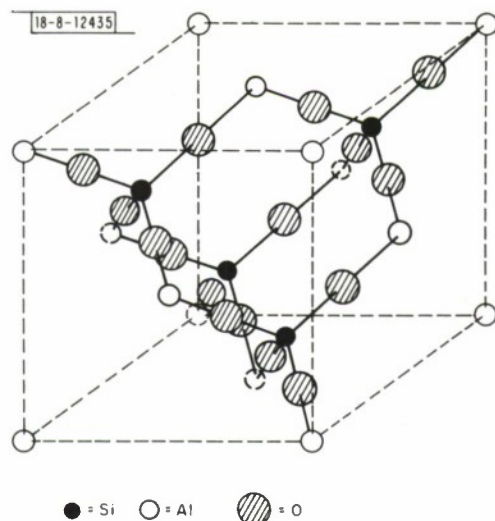
3

Fig. I-4. The AlSiO$_4$ subarray of carnegieite.

$\bullet$ = Si $\bigcirc$ = Al   ◍ = O

Note that, in the idealized structure, the O^{2-}-ion array is half as dense as a cubic-close-packed array. It can be derived from the close-packed array by removal of alternate [110] or [1$\bar{1}$0] rows.

B.   SAMPLE PREPARATION

1.   Hot-Pressed Ceramic Disks

Transport measurements are made on dense, polycrystalline ceramic disks approximately 1/2 inch in diameter and 0.05 to 0.1 inch thick. Densities in excess of 90 percent, and preferably 95 percent, of theoretical are required for proper material evaluation.

There is no general method for obtaining disks of very high density. The method chosen in each case depends necessarily on the properties of the particular material. Some of the more important properties that must be considered are stability and particle size.

a.   Thermal stability. If a material can be heated to temperatures near the melting point ($T/T_{melt} > 0.75$), high densities can be achieved even without pressure. If high temperatures cannot be used to achieve densification, high pressure and/or a flux may be required.

b.   Chemical stability. To prevent a material from being either oxidized or reduced, it may be necessary to use special dies and pistons as well as a controlled atmosphere.

c.   Phase stability. Some idea of the T-P phase diagram for a material is important. At the extreme conditions used in hot pressing, phase transformations are common. This is especially true of many of the metastable phases considered in this investigation. Lack of thermal stability may call for high pressures for densification, and high pressures may promote phase transformations.

d.   Particle size. Some materials resist high densification unless the initial particle size is very small (<1μm).

We have developed three hot-pressing stations capable of operating to about 1200°C. One of these is a vacuum or controlled-atmosphere station. These systems employ dies and pistons of various types: ceramic, graphite, steel, tungsten carbide. We also have hydrostatic-pressure equipment capable of preforming a sample and binder to 30,000 atmospheres and subsequently firing to 1700°C.

4

2. Powder Preparation

Powder samples are prepared by conventional methods.

Metastable phases may be prepared either by high pressure or by ion exchange.

C. TRANSPORT MEASUREMENTS

1. Ionic Conductivity

Ionic conductivity is generally measured on ceramic disks with an AC vector-impedance meter (5 Hz to 500 kHz) and the use of both blocking and non-blocking electrodes. The blocking electrodes permit electron transport, but restrict ion transport to a displacement current. The non-blocking electrodes consist of a coating of colloidal graphite on both sides of the sample. Because Na^+ ions can be discharged into such electrodes, polarization is avoided at higher frequencies and is often trivial even at frequencies as low as 500 Hz. In the lower resistance ranges, the impedance meter applies a sinusoidal potential of about 2.7 mV rms and yields a simultaneous readout of impedance and phase angle.

For comparison purposes, some DC and low-frequency AC measurements are made with molten $NaNO_3$ on both sides of the specimen. These molten-salt measurements have been in good agreement with data obtained with the "reversible" graphite electrodes. Of course, the only truly reversible electrodes would be molten sodium. However, interface problems make the sodium electrodes less useful in normal evaluation studies. The graphite electrodes are useful because, while not reversible, they are "non-polarizing."

2. Voltage Pulse with Blocking Electrodes

In order to investigate the ionic conductivity in more detail, we have devised an unconventional measurement procedure.

Samples are placed between sheets of gold foil, which serve as blocking electrodes. Trains of pulses of alternating polarity (in order to avoid permanent polarization of the sample) separated by quiescent intervals are applied to the electrodes. The pulse risetime is approximately 100 nanoseconds, the amplitude can be varied from 0.1 to 10 volts, the width from one millisecond to 5000 seconds, and the duty cycle from 12 to 100 percent.

Wide pulses are used to test for the presence of electron conductivity. Ions cannot pass through the gold electrodes, and hence the external current that flows to balance the charge of the ions collected near the electrodes must eventually die out. However, electrons can pass through the gold and, if mobile in the sample, will give rise to an additional external current that will not die out. The ionic current decays so slowly that extremely long waits would be required to eliminate the possibility of electron conduction, but reasonable pulse widths suffice to show any electronic component to be several orders of magnitude less than the ionic conduction.

In addition, we hope to gain insight into the process of ion transport by studying the current as a function of time measured from the start of the voltage pulse. The current is sampled by a gated amplifier whose gate is swept through the time duration of the voltage pulse. The output is compressed by a logarithmic converter and is plotted on an x-y recorder against the time of the gate.

The blocking electrodes must behave like capacitors (no real ionic current can flow through them), and the electrolyte is expected to behave like a resistor. Given our experimental conditions, the graph of the logarithm of the current versus time of a resistance-capacitance circuit

would be a straight line, which our data are not. However, assuming the resistance of the electrolyte to be a constant R, one obtains initially

$$V = Ri(o) \quad ,$$

where V is the voltage across the sample, and subsequently

$$V = Ri(t) + \frac{Q(t)}{C_{eff}} = Ri(t) + \frac{1}{C_{eff}} \int_0^t i(t')dt' \quad ,$$

so that

$$RC_{eff} = \frac{1}{i(o) - i(t)} \int_0^t i(t')dt' \quad .$$

We have calculated this quantity from our data. We find $\log(RC_{eff})$ to be linear in log time with a slope close to 0.5 over several decades of time. Preliminary results indicate that the linear range is larger with denser samples and that it extends to shorter times with β-alumina than for $NaSbO_3 \cdot (1/6)$ NaF.

The observed increase in C_{eff} with time is inconsistent with any straightforward model in which a homogeneous current carries charge from one side of the sample to the other. There is hope that it can be understood in terms of statistical local fluctuations (inhomogeneities) in such a current. Such fluctuations would cause internal charge accumulations that behave like capacitors in series. Dispersal of these accumulations removes the potential drop across their capacitances, thus reducing the total drop associated with the external charge Q(t), which is equivalent to an increase in $C_{eff}(t)$. The presence of grain boundaries could interfere with the dispersal of internal charge accumulations, and hence affect the time dependence of C_{eff}.

D. RESULTS

1. Antimonates

a. NaSbO_3. An isomorphous, metastable "$NaSbO_3$" phase having the cubic Im3 structure was obtained by ion exchange, the high-pressure Im3 phase of $KSbO_3$ or of $TlSbO_3$ being immersed for a few hours in molten $NaNO_3$. Single-crystal structure analysis, obtained by ion exchange of a crystal of $TlSbO_3$, located the Na^+ ions randomly distributed among the octahedral M_1 and M_2 sites of Fig. I-2.[7] This analysis produced three significant findings:

(1) The apparent sodium concentration is in excess of stoichiometry, suggesting a chemical formula $Na_{1+x}SbO_3$ with $x \approx 0.29$.

(2) There is no electron density in the tunnel intersections at the origin and body-center positions.

(3) In the disordered Im3 phase, Na^+-Na^+ separations of only 2.303 Å must occur, especially as the occupancy factors of the M_1 and M_2 sites were in the ratio 0.82/0.29 rather than 2/1.

In the absence of detailed chemical analysis, the apparent excess sodium obtained by x-ray analysis could be at least partially due to an incomplete exchange of the heavier Tl^+ ions by Na^+ ions. In our early work, we used only a single ion-exchange bath.

High pressure stabilizes the cubic Im3 phase of $KSbO_3$ because this phase is more dense than the ilmenite phase. For $NaSbO_3$, the situation is reversed, which limits the pressure that

6

can be applied for densification of the metastable, cubic $NaSbO_3$. Because it is metastable, the temperature that can be used for densification is also limited. Nevertheless, we have been able to obtain specimens of 92 to 98 percent theoretical density by using a $NaNH_2$ fluxing agent. A mixture of fine (<1 μm) powder and 2 weight percent $NaNH_2$ is placed in a tungsten-carbide die-and-piston assembly. The system is evacuated to pressures less than 1 μm. A pressure of 30,000 psi is applied, the temperature is raised to 600°C and held for an hour or so; the pressure is then released and the specimen allowed to cool. After removal, the specimen is baked out in a vacuum at 500°C.

Conductivity measurements showed no measurable electronic contribution and an ionic resistivity at 300°C of $\rho_{300} = 18$ Ω-cm at 1000 Hz with graphite electrodes. The fact that this resistivity is only a factor three larger than that of the best β-alumina samples at 300°C demonstrates the validity of the skeleton-structure concept.

b. **$NaSbO_3 \cdot (1/6)$ NaF.** Since the tunnel-intersection sites are empty in $NaSbO_3$, it suggests that they repel positive ions. If so, the Na^+ ions jump from M_1 site to M_1 site without passing through the tunnel intersections. This would mean that placement of an anion at the intersection sites could stabilize the cubic $KSbO_3$ structure, thus explaining Spiegelberg's stabilization of the Pn3 phase of $KSbO_3$ by annealing for 3 weeks at 1000°C in a porcelain crucible.

A telephone communication, which hinted that anion substitutions might stabilize $KSbO_3$ at atmospheric pressure, from R.S. Roth of NBS led us to investigate $KSbO_3 \cdot (1/6)$ KF. Roth independently tried stabilization of $KSbO_3$ by fluorine substitutions, and reported[8] the atmospheric-pressure preparation of $K_{1-x}SbO_{3-x}F_x$. Since he failed to report any chemical analysis, it is probable that his phase was also $KSbO_3 \cdot (1/6)$ KF. We were interested not only in the possibility of eliminating a high-pressure step in the preparation of $NaSbO_3 \cdot (1/6)$ NaF, but also in whether the existence of an anion at the tunnel intersections would aid or hinder Na^+-ion mobility.

The precursor $KSbO_3 \cdot (1/6)$ KF was prepared by firing a 2:1 weight ratio of $K_2H_2Sb_2O_7 \cdot 4H_2O$ and KF at 900°C for 2 hours. Subsequent leaching of the product removed the excess KF, leaving the compound $KSbO_3 \cdot (1/6)$ KF. This compound was immersed in molten $NaNO_3$ at 325°C for 2 hours and then water leached. Three such treatments yielded a pure product, identified by both chemical and structural analysis[9] as $NaSbO_3 \cdot (1/6)$ NaF. The F^- ions occupy the tunnel-intersection sites of the Im3 structure, and the Na^+ ions are randomly distributed on the octahedral M_1 and M_2 sites. The shortest Na-Na distance, between M_1 sites of neighboring tunnels, is here 2.87 Å.

Although $NaSbO_3 \cdot (1/6)$ NaF has moderate temperature stability, it cannot be heated to temperatures near the melting point. Therefore, high pressures are required for densification. However, at 5000 atmospheres and 600°C, there is partial disproportionation and transformation to the more dense ilmenite phase of $NaSbO_3$. Consequently, the densification procedures used for $NaSbO_3$ specimens were also employed for $NaSbO_3 \cdot (1/6)$ NaF samples.

Figure I-5 shows a plot of resistance vs $1/T$ for a typical specimen of $NaSbO_3 \cdot (1/6)$ NaF. The slope yields an activation energy of ~ 0.35 eV for a Na^+-ion jump. This is about a factor two larger than that found for β-alumina. However, the preexponential factor is smaller, which means that $NaSbO_3 \cdot (1/6)$ NaF has a smaller resistivity than β-alumina at higher temperatures. The difference in preexponential factors reflects, presumably, the fact that the entire volume of $NaSbO_3 \cdot (1/6)$ NaF participates in Na^+-ion conduction. Comparison of three different measurement techniques gave $\rho_{300} = 13$, 17, and 18 Ω-cm, respectively, for graphite electrodes and 1000 Hz, molten $NaNO_3$ electrodes and 1000 Hz, and molten $NaNO_3$ with DC.
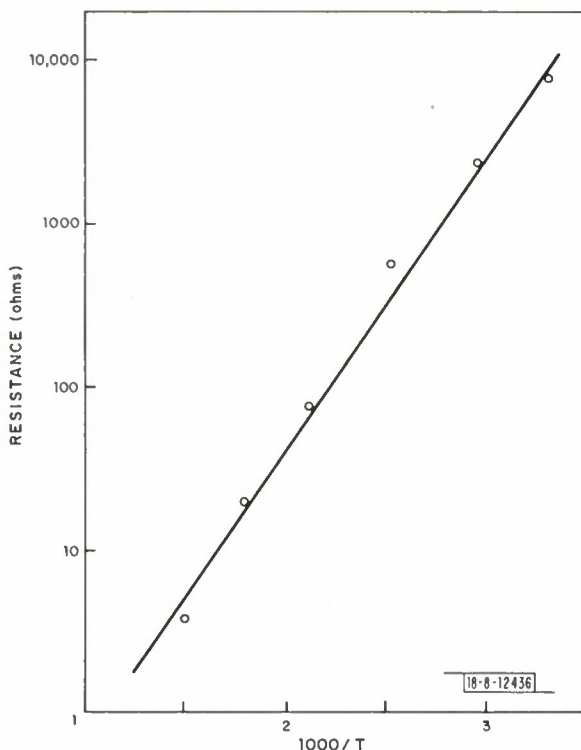
Fig. I-5. Resistance vs 1/T for a typical specimen of $NaSbO_3 \cdot (1/6)$ NaF.

From Fig. I-5 we deduce three conclusions: (1) cubic skeleton structures have the improvement in preexponential factor anticipated for bulk vs layer Na^+-ion conduction, (2) placement of an anion at the tunnel intersections does not impede the Na^+-ion mobility, thereby confirming that the Na^+ ions avoid these positions in $NaSbO_3$, and (3) reduction in the Na^+-ion activation energy for hopping, which might be achieved, for example, were occupancy of the M_1 and M_2 sites equivalent, could make the transport properties of cubic skeleton structures superior to those of β-alumina.

2. Pyrochlores

Initially, we prepared the defect-pyrochlore $KTaWO_6$ by conventional ceramic techniques. A nominal $NaTaWO_6$ was prepared by ion exchange in molten $NaNO_3$. The resistivity of this compound was about a factor ten larger than that of $NaSbO_3 \cdot (1/6)$ NaF, but still low enough to be interesting. Because W^{6+} ions would be reduced to W^{5+} ions by molten sodium, we turned to a study of the chemically more stable pyrochlore $A^+Ta_2O_5F$. In this study[10] we found that the pyrochlores may be hydrated, and a subsequent investigation of nominal $NaTaWO_6$ showed it to be, in fact, partially hydrated: $NaTaWO_6 \cdot xH_2O$ with $x \approx 0.5$.

The compound $RbTa_2O_5F$ can be synthesized directly. Equal amounts of dry RbF and reagent-grade Ta_2O_5 were mixed in a crucible and fired at 750°C under an argon atmosphere for 2 days. Regrinding and refiring two times produced single-phase powders. Single crystals of $RbTa_2O_5F$ were prepared by addition of excess RbF as a flux. In one run, a 4:1 molar ratio of RbF and Ta_2O_5 was fired at 1150°C for 30 minutes and quenched. The product contained crystals about 0.1 mm across.

The K and Na analogs could not be synthesized directly. If $RbTa_2O_5F$ is placed in molten KNO_3, the product of ion exchange is KTa_2O_5F. However, on exposure to air it becomes

8

hydrated to $KTa_2O_5F \cdot H_2O$. The lattice parameter of $RbTa_2O_5F$ is 10.496 Å, of $KTa_2O_5F \cdot H_2O$ is 10.605 Å. TGA measurements showed a reversible, broad transition, from 50 to 200°C, having a weight loss of one H_2O molecule per KTa_2O_5F molecule. Although our measurements on powder samples showed an amorphous dehydration product, a repeat of our experiment by R.S. Roth of NBS gave a cubic lattice parameter a = 10.49 Å, somewhat smaller than that of the hydrated compound but anomalously large relative to the parameter for $RbTa_2O_5F$. This finding suggests that the K^+ ions are not restricted to the large 8b sites, as are the Rb^+ ions, but occupy — at least partially — the 16d positions. A single-crystal x-ray study of $KTa_2O_5F \cdot H_2O$ revealed electron density of both the 16d and 8b sites in a ratio 2.5:1, and it was not possible to distinguish whether the water on the K^+ ions occupied the 8b positions preferentially.

Attempts to prepare $NaTa_2O_5F$ by ion exchange of $RbTa_2O_5F$ in molten $NaNO_3$ yielded incompletely exchanged products. However, ion exchange first with K^+ ions and then with Na^+ ions did yield a completely exchanged product. Although chemical analysis gave a Rb:Ta and a K:Ta ratio of 1:2, as anticipated, the Na:Ta ratio is x:2, where $x \approx 2$. These same Rb:Ta and K:Ta ratios were obtained on reversing the ion exchange. Moreover, structural analysis gave an apparent Na^+-ion excess equivalent to $x \approx 3$. We thought this discrepancy might be due to the presence of OH^- ions, giving $Na_2Ta_2O_5F \cdot OH$, but neither IR data nor TGA experiments nor the preparation of "$NaTa_2O_5F$" from anhydrous KTa_2O_5F gave any evidence of the presence of OH^- ions. Since electrical measurements gave no measurable electronic component, the excess sodium appears to be charge compensated by some anion — presumably O^{2-} ions.

Preparation of hot-pressed, ceramic disks is complicated by the fact that both pressure and temperature induce disproportionation to the perovskite $NaTaO_3$ and TaO_2F. Specimens approaching 82 percent theoretical density were prepared by the same procedures used to obtain pellets of $NaSbO_3$. A $\rho_{300} \approx 150$ Ω-cm was obtained with graphite electrodes and 1000 Hz.

Examination of the defect-pyrochlore fluorides prepared by Babel et al.[5] reveals that the Rb and Cs compounds, which have A^+ ions only in 8b sites, are dehydrated. The K compounds, on the other hand, are only dehydrated if the lattice parameter is small enough to retain the K^+ ions in 8b sites ($KNiAlF_6$ with a = 9.92 Å). Compounds with larger lattice parameters are hydrated: $KNiCoF_6$ has a = 10.18 Å and $KNiCoF_6 \cdot H_2O$ has a = 10.45 Å, $KCoCrF_6 \cdot H_2O$ and $KNiVF_6 \cdot H_2O$ are only reported with the hydrated parameters a = 10.48 and 10.51 Å. These findings suggest that there may be a critical lattice parameter at which the K^+ ion has the same preference for 8b and 16d sites. This should be the optimum parameter for fast K^+-ion conduction. Unfortunately, it may be difficult to determine this critical parameter because the critical parameter for hydration occurs at a smaller cell size.

Ion exchange of $RbMgAlF_6$, a = 9.94 Å, gives dehydrated $KMgAlF_6$ with a = 9.86 Å and a non-cubic "$NaMgAlF_6$" (which can be reverse ion exchanged).

The transport properties of these fluorides have yet to be determined.

3. Aluminosilicates

Work on the aluminosilicates is, at this time, very preliminary. Because cubic $NaAlSiO_4$ is unstable at room temperature, the related stable compounds $Na_4Al_2Si_2O_9$ and $Na_3Al_2Si_2O_{8.5}$ were prepared. These have the $NaAlSiO_4$ structure of carnegieite, but with excess Na_2O. The position of excess O^{2-} ions has not been determined. Transport measurements on disks of ca. 75 percent density gave a $\rho_{300} \approx 110$ and 1900 Ω-cm, respectively, for the two compounds with graphite electrodes and 1000 Hz.

REFERENCES

1. Y. F. Yao and J T. Kummer, J. Inorg. Nucl. Chem. 29, 2453 (1967).

2. R. Ridgeway, A. Klein, and W. O'Leary, Trans. Electrochem. Soc. 70, 71 (1936).

3. P. Spiegelberg, Ark. Kemi 14A, 1 (1940).

4. J. A. Kafalas, Solid State Chemistry, Proc. 5th Materials Res. Symp. Inst. Materials Res., NBS Oct. 18-21, 1971, R. S. Roth and S. J. Schneider, Jr., eds. (U.S. Dept. Commerce, 1972), p. 287; J. B. Goodenough and J. A. Kafalas, J. Solid State Chem. 6, 493 (1973).

5. D. Babel, G. Pausewang, and W. Viebahn, Z. Naturforsch. 22b, 1219 (1967).

6. J. Singer, private communication.

7. H. Y-P. Hong, J. A. Kafalas, and J. B. Goodenough, J. Solid State Chem. 9, 345 (1974).

8. W. S. Brower, D. B. Minor, H. S. Parker, R. S. Roth and J. L. Waring, Mater. Res. Bull. 9, 1045 (1974).

9. H. Y-P. Hong, J. A. Kafalas, J. B. Goodenough, C. H. Anderson, Jr., and D. M. Tracy, Solid State Research Report (1974:2), Lincoln Laboratory, M.I.T. (15 May 1974), p. 20, DDC-AD 783634/9.

10. J. B. Goodenough, H. Y-P. Hong, and J. A. Kafalas, Solid State Research Report (1974:3), Lincoln Laboratory, M.I.T. (15 August 1974), p. 32, DDC-AD-A001595.

II. PHOTOELECTROLYSIS

A.   INTRODUCTION

Our work has emphasized the use of semiconducting rutile TiO_2 as the working photocatalytic electrode for achieving the photoelectrolysis of water.   The main reason for this is the fact that TiO_2 is the lowest gap n-type semiconductor that, under illumination at an interface with water, evolves O_2 and does not decompose.   All the well-known semiconductors, such as Ge, Si, CdS, GaAs, and ZnO are not chemically inert, but rather dissolve under anodic polarization.   In contrast to the earlier research of Fujishima and Honda[1] with single-crystal electrodes, our research has been carried out with n-type hot-pressed TiO_2 powders which are less expensive and easier to fabricate than single crystals.   We have investigated the physics and electro-chemistry of a photoelectrolysis cell consisting of ceramic n-type TiO_2 as the anode and platinized-platinum as the cathode.   By a correlation and analysis of the experimental data, the parameters of the system were adjusted so that the reaction at the TiO_2 was made the rate-limiting step; the system was then optimized by appropriately bending the bands in TiO_2 and shifting the Fermi level of the ions in the solution so as to maximize the efficiency of the cell. The external quantum efficiency was determined under these conditions.

B.   FUNDAMENTAL CONSIDERATIONS

1.   Basic Operation

Figure II-1 shows an energy diagram of a photoelectrolysis cell consisting of a semicon-ductor (as the working electrode), an electrolyte, and platinum (as the counter electrode).   The energy bands of the semiconductor are bent at the surface because of the difference in work functions between the semiconductor and the electrolyte, so that at the interface the analog of a Schottky barrier exists.   In the center, in the electrolyte, are shown the mean-free energies for the reactions taking place, namely, the evolution of O_2 at the semiconducting anode and H_2 at the cathode.   In this arrangement, the semiconductor surface is irradiated by photons of energy at least equal to that of the energy gap. The resulting hole-electron pairs do not
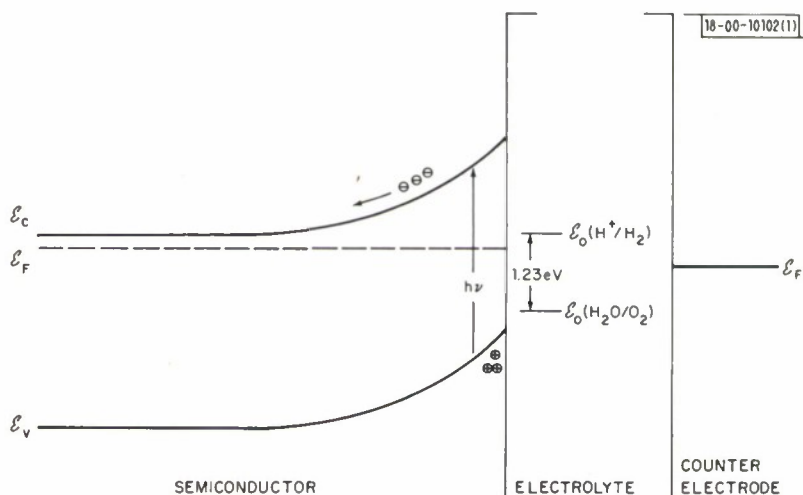

Fig. II-1.   Energy diagram of a photoelectrolysis cell.

recombine but are separated by the electric field of the barrier; the electrons move away from the surface to the bulk and through the external circuit to the cathode where they discharge H_2 ($2e^- + 2H^+ \rightarrow H_2$), and the holes remain at the surface of the semiconductor where they can interact with the electrolyte to produce O_2 [$2p^+ + H_2O \rightarrow (1/2) O_2 + 2H^+$]. The overall chemical reaction of this system is

$$2h\nu + H_2O \rightarrow \tfrac{1}{2} O_2 + H_2 \tag{1}$$

provided the semiconductor is chemically inert, serving only to absorb energy from the light and to produce the holes and electrons that make the reaction possible.

2. Flat-Band Potential

As has been discussed above, a necessary condition for efficient operation of photoelectrolysis is the bending of the energy bands at the semiconductor-electrolyte interface. This band bending separates the holes and electrons, thus preventing their recombination and making them available to discharge ions at the solid-liquid interface. Two techniques have been used for measuring this band bending: (1) capacitance vs electrode voltage, and (2) surface photovoltage vs electrode voltage.

### a. Capacitance vs Electrode Voltage

The upward band bending, as shown in Fig. II-1, corresponds to the existence of a positive space charge of donor ions in the semiconductor near the interface. It is customary to simplify the problem to the case of completely ionized donors of density N_D per cm^3. The potential distribution within the semiconductor space-charge region is then obtained from Poisson's equation. Mott[2] and Schottky[3] first showed that the potential distribution is parabolic with distance. The derivative of the charge with respect to potential gives the differential capacitance, C, which can be written in the form

$$\frac{1}{C^2} = \frac{2}{e \epsilon \epsilon_o N_D A^2} (V - V_{FB}) \quad , \tag{2}$$

which is commonly called the Mott-Schottky expression. Here e is the electronic charge, ϵ_o is the free-space permittivity ($=10^{-11}/36\pi$),* ϵ is the relative permittivity, A is the area of the electrode (in cm^2), and V_{FB} is the flat-band potential (i.e., the potential of the semiconductor electrode with respect to some reference electrode, commonly the saturated calomel electrode, SCE, for which the bands are not bent but lie flat from the interior right up to the surface). The band bending can be obtained from V_{FB} since applied-voltage changes do not shift the solution redox levels (for solutions of 0.1 N and higher) relative to the bands at the semiconductor surface. For the case of no surface states, Eq. (2) also gives the bulk electron density, N_D. Figure II-2 is a Mott-Schottky plot for one of our TiO_2 hot-pressed disks taken at a pH = 8. The intercept of this straight line gives a flat-band potential of −0.72 eV relative to SCE. The slope of this line normally yields the electron density, N_D. Unfortunately, the surface area of a pressed powder electrode is not equal to the geometric area. Even for single crystals a surface roughness of 1.5 to 2 is found. For the case of powders, this factor may run from 10 to 100 so that only an estimate of the electron density of between $10^{18}/cm^3$ to $10^{22}/cm^3$ can be made. A Hall effect measurement would pin this number down.

---

*With this value for ϵ_o, length is in cgs units and the capacitance is in farads.

Fig. II-2. $1/C^2$ vs V relative to SCE at pH = 8. Note the straight-line behavior as predicted by the Schottky-Mott theory. The geometric area of the hot-pressed TiO_2 disk = 1.26 cm^2.
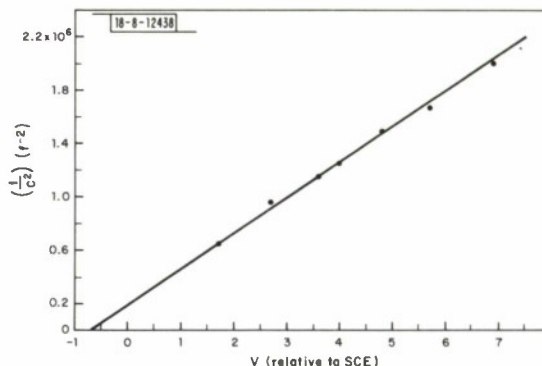
b.   Surface Photovoltage vs Electrode Voltage

Again consider the bands bent upwards as in Fig. II-1. The hole density at the surface p_s is given by $p_s = p_B\, e^{+e\Psi/kT}$ where p_B is the hole density in the bulk and $e\Psi$ is the amount of band bending. Illumination of the semiconductor surface with light of energy $h\nu > \mathcal{E}_g$ produces hole-electron pairs, $\Delta p = \Delta n$.

When these non-equilibrium carriers are created, the material becomes more intrinsic, and the band edges shift to place the Fermi energy $\mathcal{E}_F$ more nearly in the center of the gap. However, at the surface the band edges are pinned by the chemical affinity. The closer the band edge is to $\mathcal{E}_F$, the more strongly it is shifted by the creation of non-equilibrium carriers. The light penetrates beyond the thickness of the space-charge region, the Debye length L_D, in which the bands are bent. Therefore non-equilibrium charge carriers are created in the bulk beyond L_D, and the band edges become flatter. Because the light penetration is finite, $\mathcal{E}_F$ must stay close to the band edge far from the surface, which represents a potential difference across the semiconductor made possible by the separation of holes and electrons because of band bending. This potential difference, which disappears if the bands are flat, is called the surface photovoltage $\Delta\Psi$.

The electrode voltage is measured relative to SCE, the potential of the saturated calomel electrode. SCE is 0.24 volt more positive than the electrochemical potential of the liquid. Application of a voltage that flattens the bands in the semiconductor increases the capacitance of the space-charge region relative to the capacitance of the Debye-Hückel layer at the counter electrode, where the potential drop across the liquid is concentrated. $\Delta\Psi$ vanishes where the bands are flat because, under these conditions and in the absence of surface states, $\mathcal{E}_F$ in the semiconductor is everywhere equidistant from the band edges. This technique is illustrated in Fig. II-3 for a pressed powder TiO_2 sample in an electrolyte of pH = 0, where the flat-band potential (zero-intercept) is determined to be —0.24 eV relative to SCE. With zero applied voltage, the TiO_2 electrode when short circuited to the platinized-platinum counter electrodes assumes a potential = +0.55 eV, relative to SCE, which gives a band bending $e\Psi = 0.79$ eV.

Of the two techniques discussed above, the capacitance voltage measurements are slower and more tedious. Consequently, for our purposes most of the measurements of the flat-band potential vs pH were taken using the surface photovoltage technique. This variation with pH is shown in Fig. II-4. The slope of the line is very close to 0.059 [pH] = (e/kT) [pH] = $(e/kT) \ln H^+$, to be expected if the main effect of the pH change is to vary the Fermi level in the solution.[4]

13
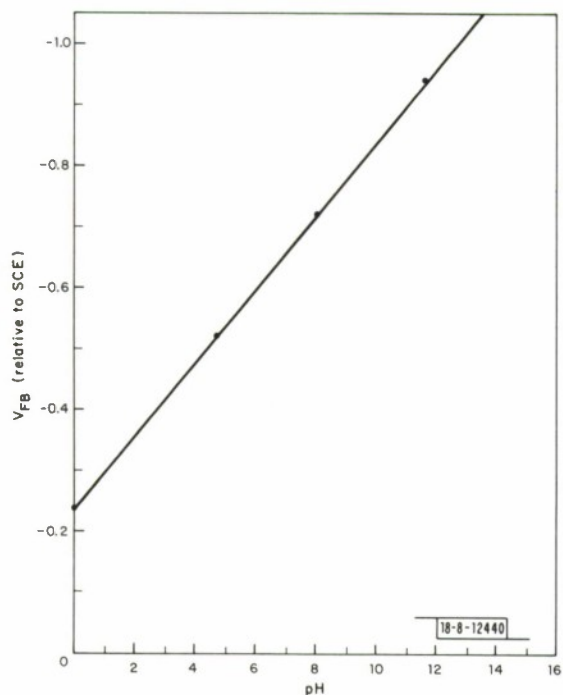
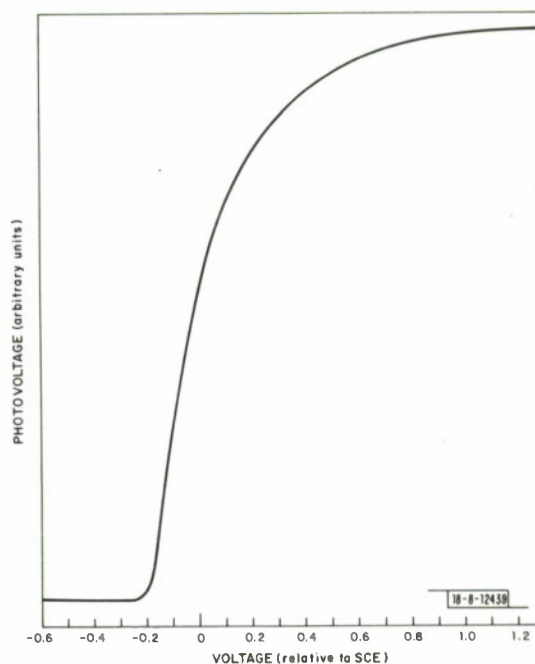Fig. II-3. Surface photovoltage vs V relative to SCE at pH = 0.

Fig. II-4. Variation of flat-band potential V_{FB} (relative to SCE) with pH.
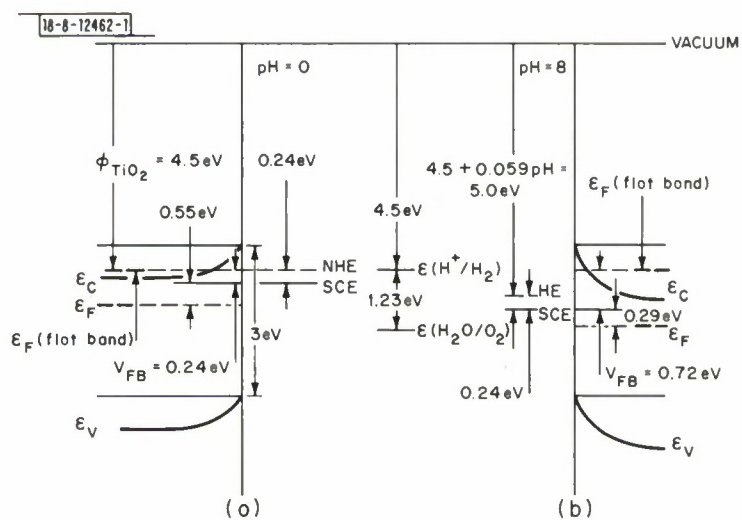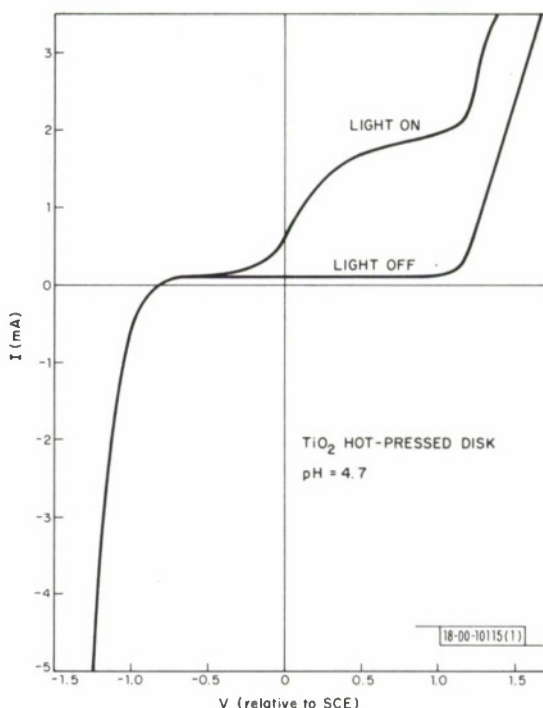

Fig. II-5. Energy diagrams of the TiO_2-electrolyte system at (a) pH = 0 and (b) pH = 8. Note that the band bending is greater at the higher pH.

Fig. II-6. Current-voltage behavior for a cell consisting of a TiO_2 working electrode and a platinized-platinum counter electrode. Note the large current increase under illumination when the TiO_2 is anodically polarized.

3. Energy Diagrams

In the absence of surface states, drawing of an energy diagram requires knowledge of the flat-band potential of the semiconductor-electrolyte system, the redox potential of the reaction at the interface (1.23 eV for the electrolysis of water), the work functions of the two components, and the energy gap of the semiconductor (3 eV for TiO_2). Because $V_{FB} = -0.24$ eV relative to SCE (at pH = 0), the flat-band Fermi energy $\mathcal{E}_F$ (flat-band) is at the same energy as the electrochemical potential of the liquid $\mathcal{E}(H^+/H_2)$. At pH = 0, $\mathcal{E}(H^+/H_2)$ is, by definition, the potential of the normal hydrogen electrode, NHE. Therefore we measure a work function for the liquid $\mathcal{E}(H^+/H_2)$, equal to the work function of TiO_2, $\varphi(TiO_2) = 4.5$ eV. This value for $\mathcal{E}(H^+/H_2)$, is in agreement with the estimates of Noyes[5] and Lohman.[6] The diagram of Fig. II-5, which neglects surface states, was drawn by using the value 4.5 eV for the work function of the TiO_2 pellets. This is the value measured in air by the Kelvin method.* Similar reasoning gives the energy diagram for pH = 8, Fig. II-5(b).

4. Current-Voltage Behavior

It is presently believed that the mechanism for electron transfer between a semiconductor and a redox electrolyte is that of tunneling between levels at the same energy in the semiconductor and the electrolyte.[7] Thus the occupied electronic states in one phase need to line up with the empty electronic states in the phase. An examination of the energy diagram in Fig. II-5 indicates that although the discharge of H_2 is energetically possible at the cathode, the discharge of O_2 at the anode will not be very effective unless this discharge takes place via levels (surface states or traps) lying within the energy gap. The fact that we do get current-voltage curves with light, such as shown in Fig. II-6, with large currents under weak anodic polarization confirms this supposition. More work needs to be done to identify, understand, and exploit further these levels.

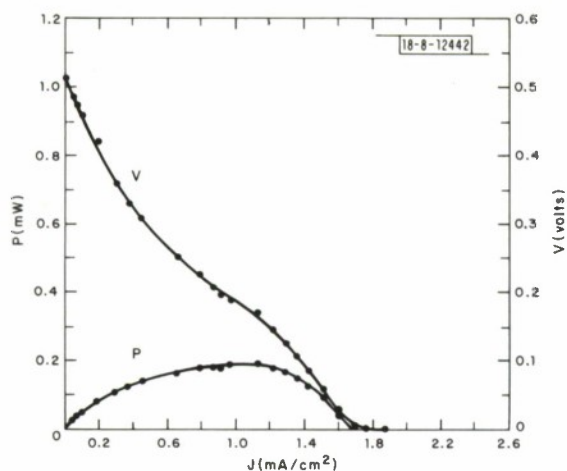*The contact potential was measured relative to Au; the work function of Au was taken as 4.68 eV.

Fig. II-7. Operating characteristics of a photoelectrolysis cell. Shown here are the variation of output voltage, V, and power, P, (to an external load) with current density, J. Electrolyte pH = 0.

Fig. II-8. Variation of short-circuit current density of photoelectrolysis cell with cathode area. The area of the TiO₂ working electrode = 1 cm². Electrolyte pH = 0.
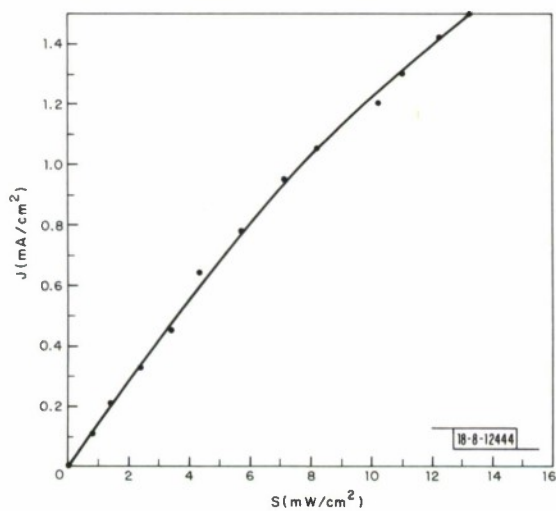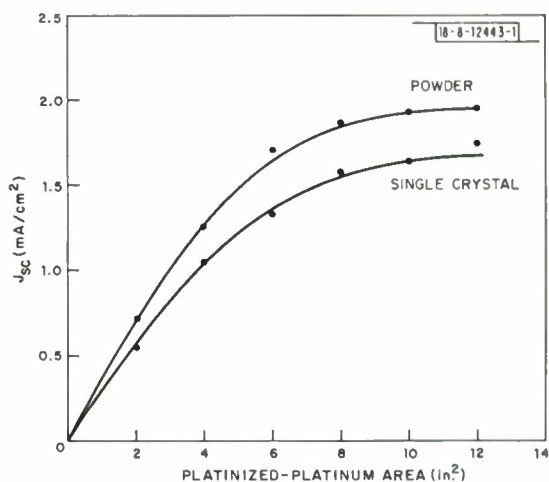
Fig. II-9. Plot of short-circuit current density of the photoelectrolysis cell vs incident light intensity at hν ≈ 4 eV. Electrolyte pH = 8.

C. PHOTOELECTROLYSIS CELL

1. Operating Characteristics and Rate-Limiting Reaction

Since, for an n-type semiconductor, a positive space-charge layer separates the holes and electrons, the photoelectrolysis process should be maximized at high pH values where the band bending is large. To check this prediction, operating characteristics under constant light irradiation (from a 150-watt Xenon source), such as shown in Fig. II-7 for pH = 0, were measured at various values of pH. The upper curve gives the output voltage, V, as a function of the current drawn from the cell. The lower curve gives the electrical power, P, extracted by the load. For maximum photoelectrolysis the cell is operated in the short circuit mode, with I_{sc} = 1.88 mA. However, it is possible to operate the cell at $I < I_{sc}$ so as to extract electrical power at the same time as gas is discharged. These two curves can be fit to a fairly good approximation by a model that considers the photoelectrolysis cell as a constant-voltage source in series with an internal resistance. In the configuration of Fig. II-7, the open circuit voltage is 0.52 volt and the internal resistance is ~350 Ω.

With our initial cell, which had a platinized-platinum (cathode) surface area about 13 times greater than the TiO_2 surface area, a study of the variation of the short-circuit current with pH produced the unexpected result that the current was a maximum at pH = 0, where the band bending is the smallest. Since a pH = 0 corresponds to a maximizing of the H^+ ions, this suggested that the discharge of H^+ ions at the cathode was the rate-limiting step in the cell. Measurements of the variation of the short-circuit current as a function of the cathode area, shown in Fig. II-8, indicated that this was indeed the case. After a sufficient increase in area of the counter electrode, the pH was again varied and higher currents were obtained at the higher values of pH. Above a pH of 4.7, the variation with pH essentially flattened out. Thus, the cell can operate with maximum efficiency at a pH around 7 or 8, i.e., with a neutral solution.

2. Current Saturation with Light Intensity

Another parameter that was investigated was the variation of the short-circuit current with light intensity. The results obtained for one pressed-powder sample are given in Fig. II-9. Here, a monochromatic source of light was used with photons at $h\nu \sim 4$ eV, which is at the energy of peak response of the cell. It will be noted that the curve of current density vs light intensity is linear at low intensity, but bends over at the higher intensities. Earlier curves, taken without a monochromator and therefore at still higher light intensities, have shown almost complete saturation. To bring this curve into a better perspective, it should be pointed out that the sun's radiation incident in the 4-eV region falls between 2 to 4 mW/cm^2, i.e., in the linear-response region.

3. Quantum Efficiency

Subsequent to the optimization of the various parameters of the photoelectrolysis cell, consisting of a hot-pressed disk of TiO_2 as the anode and a platinized-platinum counter electrode as the cathode, the external quantum efficiency of the cell was measured. For this purpose, the electrolysis cell was powered by a monochromatic source, consisting of a grating monochromator and a 1000-watt Xenon lamp, and the current response, J, was measured as a function of photon energy. The light intensity, S, emitted by the monochromator was measured (at each value of photon energy) by means of a thermopile power meter that had a flat response
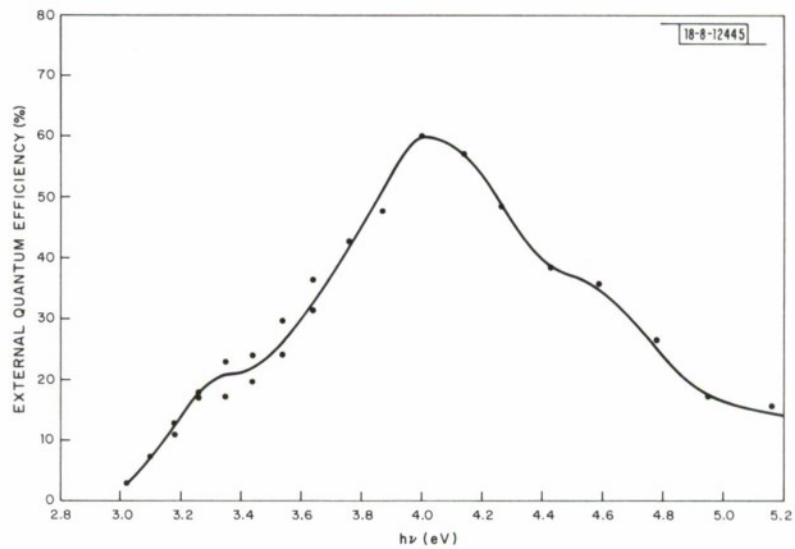
Fig. II-10.   Variation of external quantum efficiency of the photoelectrolysis cell with photon energy. Electrolyte pH = 8.
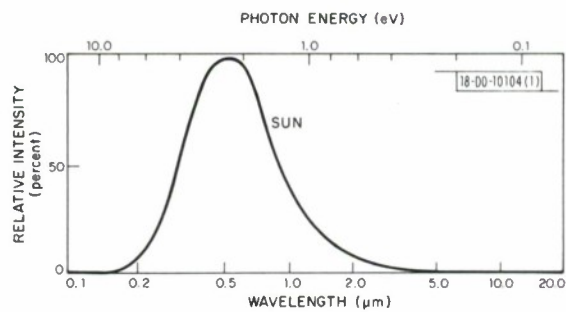
Fig. II-11.   Spectrum of the sun's radiation.

down to 0.25 μm. The external quantum efficiency, QE, defined as the ratio of number of elec-trons per second, N_e, produced in the external circuit to the number of photons per second, N_p, incident on the cell, was calculated at each value of photon energy from

$$QE \equiv \frac{N_e}{N_p} = \frac{\frac{J(amp/cm^2)}{(e\ coulombs)}}{\frac{S(watts/cm^2)}{(h\nu, eV)\ (e\ coulombs)}} \quad \frac{J(amps/cm^2)}{S(watts/cm^2)}\ h\nu(eV) \quad . \qquad (2)$$

The results of measurements of QE vs photon energy (for intensities in the linear region) are presented in Fig. II-10 for a buffered electrolyte with pH = 8. Actually above a pH ≈ 4.7, the QE varies very little. From the curve of Fig. II-10 it is evident that a maximum external quan-tum efficiency QE ~ 60 percent occurs at a photon energy $h\nu$ ≈ 4 eV. The maximum internal quantum efficiency, which takes into account reflection losses at the interfaces and absorption losses in the electrolyte, is estimated to be close to 100 percent. These results indicate that photoelectrolysis is fundamentally a very efficient process.

D. PRACTICAL IMPLICATIONS

1. Overall Efficiency

For a practical system, what is relevant is the overall efficiency of the TiO_2 photoelec-trolysis cell when driven by sunlight. Even with the large mismatch between the peak in the cell response at 4 eV and the peak at 2.4 eV of the sun's radiation (Fig. II-11), measurements using the sun as a source of photons give a QE of ~2 percent for electron generation, or ~1 per-cent for H_2 fuel generation (since $2e^- + 2H^+ \rightarrow H_2$). This is to be compared with a 15 percent efficiency for electrical energy generation from the best solar cells and ~5 percent efficiency for polycrystalline solar cells. Furthermore, the photoelectrolysis process has the advantage of converting the solar energy to chemical energy stored in a mobile, long-lived fuel.

2. Ease of Electrode Preparation

Most of the present research was performed on TiO_2 disks prepared by hot-pressing pow-dered rutile at 750°C under a pressure of 10,000 psi. The hot-pressed disks were then made conducting by reduction-heating in vacuum for three hours at ~600°C. The loss of oxygen makes the samples n-type and gives them a blue coloration. Ohmic contacts to the sample were easily prepared by using a Pt backing for the pellet during the hot-pressing process. Prelimi-nary results on thin TiO_2 films, prepared either by anodizing Ti or sputtering, appear to give similar results. Thus, in contrast to the p-n junction of a solar cell, the fabrication problem here is simpler and cheaper.

3. Approximate Cost of a TiO_2 Photoelectrolysis System

Actual measurements on the roof of Lincoln Laboratory with an elementary system indicate a current-density J = 0.54 mA/cm^2 = 5.4 A/m^2. Taking 6 hours of sunlight per day, this corre-sponds to $5.4 \times 3.6 \times 10^3 \times 1.17 \times 10^5$ coulombs or

$$\frac{1.17 \times 10^5\ coulombs}{2 \times (96,500)\ coul/mole} = 0.61\ \text{moles of}\ H_2/m^2\ \text{per day} \quad .$$

Each mole of H_2 has a chemical energy of 68.3 kcal. Thus the energy of the collected gas per m^2 is 41.6 kcal per day = 165 Btu/day = 6×10^4 Btu/year.

Although it is difficult at this time to make an exact calculation for the cost per m^2 of panel, an estimate can be made. The price for TiO$_2$ powder (even in laboratory quantities) is $2/m^2. For the counter electrode some inexpensive metal sheet, such as steel, could be platinized, but the price for the platinizing, as presently done, is high; ultimately we will be using a semiconductor as the counter electrode. In the case of a thin semiconductor film, the price would not be more than ~$3/m^2. The other component of this cell is a cover glass that will pass the sunlight; float glass costs ~$1.50/m^2. With an additional $3.50/m^2 for packaging and installation, the estimated cost of a complete TiO$_2$ panel is $10/m^2. Writing off this investment in 20 years, gives a cost for H$_2$ fuel of

$$\frac{\$10}{6 \times 10^4 \times 20} = \$8.25 \text{ per } 10^6 \text{ Btu} \quad .$$

This cost estimate is quite competitive with $9 per 10^6 Btu for electric heat:

$$\frac{10^6 \text{ Btu}}{3.4 \times 10^3 \text{ Btu/kwhr}} \times \$3 \times 10^{-2}/\text{kwhr} = \$9$$

but more expensive than the $3.20 per 10^6 Btu for fuel oil:

$$\frac{10^6 \text{ Btu}}{(2 \times 10^4 \text{ Btu/lb}) (6.5 \text{ lb/gal})} \times \$0.40/\text{gal} = \$3.20 \quad .$$

Improved efficiencies for the photoelectrolysis cell would, of course, reduce the cost even further, making hydrogen generation by solar energy a very attractive option indeed.

REFERENCES

1. A. Fujishima and K. Honda, Nature **238**, 37 (1972).

2. N. F. Mott, Proc. Roy. Soc. **A171**, 27 (1939).

3. W. Schottky, Z. Phys. **113**, 367 (1939).

4. D. I. Tchernev, to be published.

5. R. M. Noyes, J. Am. Chem. Soc. **84**, 573 (1962).

6. F. Lohmann, Z. Naturforschg. **22a**, 843 (1967).

7. H. Gerischer, "Metal and Semiconducting Electrode Processes," in The Surface Chemistry of Metals and Semiconductors, H. C. Gatos, ed. (J. Wiley and Sons, New York, 1960), p. 177.

REPORT DOCUMENTATION PAGE		READ INSTRUCTIONS BEFORE COMPLETING FORM
1. REPORT NUMBER ESD-TR-75-108	2. GOVT ACCESSION NO.	3. RECIPIENT'S CATALOG NUMBER
4. TITLE *(and Subtitle)* Solid Electrolytes and Photoelectrolysis		5. TYPE OF REPORT & PERIOD COVERED Semiannual Technical Summary 1 March through 31 December 1974
		6. PERFORMING ORG. REPORT NUMBER
7. AUTHOR(s) John B. Goodenough John G. Mavroides Kirby Dwight, Jr. James A. Kafalas Henry Y-P. Hong Dimiter I. Tchernev James A. Kafalas Donald F. Kolesar		8. CONTRACT OR GRANT NUMBER(s) F19628-73-C-0002
9. PERFORMING ORGANIZATION NAME AND ADDRESS Lincoln Laboratory, M.I.T. P.O. Box 73 Lexington, MA 02173		10. PROGRAM ELEMENT, PROJECT, TASK AREA & WORK UNIT NUMBERS ARPA Order 2696 Program Code 5D10
11. CONTROLLING OFFICE NAME AND ADDRESS Defense Advanced Research Projects Agency 1400 Wilson Boulevard Arlington, VA 22209		12. REPORT DATE 31 December 1974
		13. NUMBER OF PAGES 32
14. MONITORING AGENCY NAME & ADDRESS *(if different from Controlling Office)* Air Force Office of Scientific Research 1400 Wilson Boulevard Arlington, VA 22209		15. SECURITY CLASS. *(of this report)* Unclassified
		15a. DECLASSIFICATION DOWNGRADING SCHEDULE

16. DISTRIBUTION STATEMENT *(of this Report)*

Approved for public release; distribution unlimited.

17. DISTRIBUTION STATEMENT *(of the abstract entered in Block 20, if different from Report)*

18. SUPPLEMENTARY NOTES

None

19. KEY WORDS *(Continue on reverse side if necessary and identify by block number)*

solid electrolytes	alkali-ion transport	fast ion transport
sodium-sulfur batteries	photoelectrolysis	catalytic electrodes
water decomposition	electrochemistry	solar energy
hydrogen generation	TiO_2	

20. ABSTRACT *(Continue on reverse side if necessary and identify by block number)*

Three classes of cubic skeleton structures are explored for fast Na^+-ion transport for use as solid electrolytes in Na-S batteries. The cubic $KSbO_3$ structure consists of an $(SbO_3)^-$ skeleton having $\langle 111 \rangle$ tunnels intersecting at origin and body-center positions. $NaSbO_3$ and $NaSbO_3 \cdot (1/6)$ NaF disks of ca. 95 percent theoretical density give a Na^+-ion resistivity at 300°C of $\rho_{300} \simeq 13$ Ω-cm and an activation energy $\epsilon_A \simeq 0.35$ eV. The defect-pyrochlore structures have a B_2X_6 skeleton of corner-shared octahedra with alkali ions in 8b positions. At a critical lattice parameter, K^+ ions have an equal site preference for 8b and 16d positions, but determination of the critical parameter and exploitation of it are hampered by a critical parameter for hydration to occur. Preliminary investigations of aluminosilicates having the carnegieite structure show promise, but a $\rho_{300} \simeq 610$ Ω-cm is the best that has been achieved to date.

DD ~FORM~ 1473 EDITION OF 1 NOV 65 IS OBSOLETE
1 JAN 73

20. ABSTRACT (Continued)

We have investigated the use of inexpensive, n-type hot-pressed TiO_2 powders as the working photo-catalytic electrode for achieving photoelectrolysis of water. TiO_2 was selected because it is the lowest gap n-type semiconductor that, under illumination at an interface with water, evolves O_2 and does not decompose. A study of the physics and electrochemistry of a photoelectrolysis cell consisting of TiO_2 as the anode and platinized-platinum as the cathode led to an optimization of the parameters of the system by appropriately bending the bands in TiO_2 and shifting the Fermi level of the ions in the solution. Under these conditions an external quantum efficiency of 60 percent was measured and, from this, an internal quantum efficiency close to 100 percent was estimated.